



HAL
open science

Crushing of additively manufactured thin-walled metallic lattices: Two-scale strain localization analysis

Yanis Balit, Pierre Margerit, Eric Charkaluk, Andrei Constantinescu

► To cite this version:

Yanis Balit, Pierre Margerit, Eric Charkaluk, Andrei Constantinescu. Crushing of additively manufactured thin-walled metallic lattices: Two-scale strain localization analysis. *Mechanics of Materials*, 2021, 160, pp.103915. 10.1016/j.mechmat.2021.103915 . hal-03873524

HAL Id: hal-03873524

<https://hal.science/hal-03873524>

Submitted on 30 Mar 2023

HAL is a multi-disciplinary open access archive for the deposit and dissemination of scientific research documents, whether they are published or not. The documents may come from teaching and research institutions in France or abroad, or from public or private research centers.

L'archive ouverte pluridisciplinaire **HAL**, est destinée au dépôt et à la diffusion de documents scientifiques de niveau recherche, publiés ou non, émanant des établissements d'enseignement et de recherche français ou étrangers, des laboratoires publics ou privés.



Distributed under a Creative Commons Attribution - NonCommercial 4.0 International License

Crushing of additively manufactured thin-walled metallic lattices: Two-scale strain localization analysis

Yanis Balit, Pierre Margerit, Eric Charkaluk, Andrei Constantinescu

Laboratoire de Mécanique des Solides - CNRS - Ecole Polytechnique - Institut Polytechnique de Paris, 91128, Palaiseau, France

The response of architected structures is characterized by multi-scale kinematics, which complex relation and effect on the engineering load response is still not completely understood and therefore needs further investigations. More precisely, the lack of experimental methods enabling to provide multi-scale data remains a key issue. The paper presents an experimental and numerical analysis of crushing tests performed on thin-walled auxetic metallic lattices manufactured by Directed Energy Deposition. The work is focused on the two-scale strain localization occurring (a) at the microscopic scale of the unit cell and (b) at the macroscopic scale corresponding to the homogenized continuum. The structures of interest are defined as the extrusion of a 2D auxetic wireframe and allow the application of an adapted digital image correlation scheme dedicated to the identification of the kinematics at the two considered scales. In particular, the microscopic kinematics are studied by following the deformation of lattice crossings, while the macroscopic strains are deduced from the motion of virtual unit cell corners. The results show that the global elastic-plastic response of the lattices is completely driven by the formation of plastic hinges at specific locations, leading to characteristic deformation patterns and eventually a collective behavior of neighboring unit cells. Companion finite element computations show an excellent match with experiments and thus enable to assess the effect of modeling assumptions, unit cell geometry, strain rate and geometrical imperfections in the global response of the architecture material.

1. Introduction

Additive manufacturing (AM) permits to manufacture architected solids with targeted properties and opens new perspectives for innovative materials. Moreover, architectures can be designed on-purpose to reach properties outside the domain of natural materials (Yu et al., 2018). A particularly interesting class of architected materials are periodic lattices, defined as the periodic distribution of a characteristic unit cell consisting of interconnected straight trusses and curved branches. These specific architectures exhibit a mechanical behavior which is highly comparable to the response of open cell foams (Hutchinson and Fleck, 2006; Ashby, 2006) and can be varied by means of elementary design changes (e.g. truss connectivity or thickness, branch curvature). As a consequence, lattice structures are interesting for a wide range of target applications such as sound and vibration insulation (Chen et al., 2020; Liu et al., 2019) or energy-absorption (Yungwirth et al., 2008; Tancogne-Dejean et al., 2016; Dheyaa et al., 2018; Maskery et al., 2017; Plocher and Panesar, 2020) where a fine tuning of the behavior is necessary. Furthermore, micro-architectures optimized for

extreme properties can be obtained by topology and shape optimization procedures such as Solid Isotropic Method with Penalization (SIMP) (Philip Bendsoe and Sigmund, 2013) or homogenization method (Allaire, 2012). In these formulations, the shape is represented using pixels and voxels (Schumacher et al., 2015), level-sets (Wang et al., 2004; Nika and Constantinescu, 2019; Agnelli et al., 2020a) or directly isogeometric rods (Wang et al., 2017).

Among the range of available additive manufacturing technologies, the Selective Laser Melting process (SLM) emerged in a large number of studies on metallic lattice materials as offers a large freedom on the geometries that can be considered, as illustrated for example in (Leary et al., 2016; Dheyaa et al., 2018; Simon et al., 2008; Bradley et al., 2020; Sélo et al., 2020; Maskery et al., 2017; Harris and McShane, 2020).

The alternative investigated in this work is the Directed Energy Deposition (DED) technology. This process is defined by the ISO/ASTM 52900:2015 standard as “the additive manufacturing process in which focused thermal energy is used to fuse materials by melting as they are being deposited” (ISO/ASTM, 2015). This additive process is suitable for structural repair, printing on non-planar substrates and adding new

* Corresponding author.

E-mail address: andrei.constantinescu@polytechnique.edu (A. Constantinescu).

components. Due to its relative novelty, fewer reports on the mechanical behavior of architected structures obtained by DED can be found (Abe and Sasahara, 2019; Baranowski et al., 2019; Antolak-Dudka et al., 2019; Sohaib and MasoodRyan, 2015; Sharma et al., 2018; Li et al., 2020; Xu et al., 2020; Zhang et al., 2020).

The performances of metallic lattice structures fabricated by additive manufacturing depend on a number of parameters associated with both the unit cell geometry definition and the involved process which is the source of various geometrical imperfections (Liu et al., 2017) (e.g. strut waviness, section variations and surface roughness). The behavior of these architected materials is the result of the kinematics occurring at multiple scales (Rashed et al., 2016). Hence their global response is sensitive to the number of unit cells in the specimen (Gu et al., 2018). Moreover, the crushing behavior of such metallic lattices depends on material instabilities such as plastic localization occurring at the unit cell scale (Emmanuel Viard et al., 2020). As a consequence, the need for multi-scale analyses is a key issue in the process of understanding the relation between the subsequent scales (Rashed et al., 2016), both from numerical and experimental points of view. On the experimental side, two complementary strategies have been proposed recently: (i) the development of specific testing setups able to isolate a particular mechanism (Dassonville et al., 2020) or (ii) the use of heterogeneous tests to relate the subsequent scales (Agnelli et al., 2020b).

The present work proposes the implementation of a multi-scale experimental analysis and its application to the analysis of the crushing behavior of 316L stainless steel lattices manufactured by DED. The investigated structures are obtained by extrusion of a planar wireframe geometry inspired by results on polymer lattices obtained using SIMP and rods (see details in (Wang et al., 2019; Clausen et al., 2015)) and which will have been fabricated using a single-track path. This 2D configuration makes possible the identification of the specimen kinematics by Digital Image Correlation (DIC). These particular unit cell geometries are characterized by a negative in-plane Poisson ratio and are therefore denoted as *auxetic*. In addition, these 3 lattices have a potential application for energy-absorption during a crash for instance. That is why, the mechanical behavior of the lattices is analyzed in this work by means of a crushing test. The structural response is analyzed at two scales (Agnelli et al., 2020b): (i) the global *macroscopic* scale relating the observed engineering strain to the applied load; (ii) the local *microscopic* scale focusing on the kinematics of branches and nodes (crossings between branches). This allows to relate the observed behaviors at the subsequent scales to the global response of the specimen. In order to provide quantitative information on the structural response, an adapted DIC procedure is presented, leading to the identification of unit cell strains and crossing member rotations. Moreover, the ability to reproduce the observed macroscopic and microscopic features using a companion numerical model is demonstrated. In particular, the effect of model assumptions, cell geometry, member thickness as well as accidental wall breakages on the compressive response of the lattice specimens are studied.

The paper is organized as follows: the first section develops aspects related to the specimen fabrication: the lattice geometry, the material, the manufacturing parameters are described, followed by the analysis of the material microstructure and the characterization of the constitutive material behavior. The second section is dedicated to the experimental compression tests. After a general discussion about each specimen response, the kinematic analysis is presented. The third section presents finite element results and comparisons with experiments. Finally, a series of concluding remarks and perspectives is given.

2. Specimen fabrication

2.1. Lattice geometries

The lattice architecture of the panel specimens analyzed next is obtained by the extrusion in the vertical direction of a two-dimensional

wire pattern, obtained by the periodic deployment of an elementary unit cell. The wire-pattern has been manufactured by the single-track path of the DED machine. The elementary unit cells were extracted from (Clausen et al., 2015) and have each a particular 2D apparent Poisson ratio. Let us further note that the architecture of these unit cells stem from topological shape optimization and are optimized in order to keep an approximately constant apparent Poisson ratio up to a finite value of the macroscopic strain. Fig. 1 presents the three unit cells corresponding to *theoretical* (i.e. *as-designed*) Poisson ratios of -0.8 , -0.2 and 0.2 respectively; a front view of the respective panels is also provided. These theoretical values of the apparent Poisson ratio are used all along the text to denote the different specimens.

2.2. Manufacturing protocol

The panels were fabricated as single track structures using the Directed Energy Deposition (DED) process, implemented in a *mobile* machine from *BeAM* (Beam) equipped with a 500 W YLR-fiber laser presenting a wavelength of 1070 nm. The powder is transported by argon gas flux and delivered to the deposition region through coaxial nozzles positioned approximately 3.5 mm above the substrate surface. At this region, The focused laser features a beam spot of around 0.65 mm. The *Oerlikon Metco* 316L stainless steel powder, obtained by gas atomization, was used as material feed; its chemical and physical properties (Oerlikon) are given in Tables 2 and 3 respectively.

It is composed of spherical particles with a diameter range of 45–100 μm . Moreover, satellites can be seen on the surface of particles, a phenomenon inherent to gas atomization (Ozbilen, 1999).

The process parameters are: (i) Laser Powder = 225 W, (ii) Deposition Speed = 2000 mm/min, (iii) Powder Flow = 6.5 g/min. As a result, the obtained single-track wall thickness was approximately 0.6 mm. The lattice was manufactured on a 316L substrate plate of dimensions 100 mm \times 100 mm \times 5 mm (length, width, thickness). These dimensions constrained the number of unit cells in each specimen as trying to manufacture small cells with respect to the track thickness leads to the failure of the print. The dimensions, number of cells and density for the three specimens are presented in Table 1. A back-and-forth printing strategy was implemented: the laser path corresponding to a layer was traveled alternatively in the forward and backward direction. The spacing between subsequent layers was set to 0.12 mm.

As a result of the lattice structure, the density of the specimens is much smaller than those of the bulk material. At the end of the process, specimens were extracted from the substrate using a saw. Due to a suboptimal choice of the process parameters, the walls of the $\mu = -0.8$ specimen present flaws at several locations that are the consequence of a default propagating in the build direction during the production. The consequence of these flaws is studied in the present work.

2.3. Microstructural analysis

A detailed microstructural analysis of some single-track walls obtained with the chosen DED process parameters can be found in (Balit et al., 2020a, 2020b). In the present work, the analysis focuses on the microstructure at the crossings of tracks. In particular, two planes corresponding to the side and the top view of a crossing are considered. The results are summarized in Fig. 2 where the two obtained EBSD maps and resulting pole figures are shown.

The presented microstructure morphology is in agreement with available results concerning additively manufactured metals (Balit et al., 2020a, 2020b): (i) long epitaxial grains associated to the high temperature gradients involved in the process; (ii) a reduced crystallographic texture. More interestingly, one can notice that the crossing between laser paths does not introduces additional defects like porosities or cracks, as strongly bonded elongated grains can be seen in Fig. 2c. This suggests that the lattice walls are firmly linked, thus the deformation of crosses during the loading of the structure is associated to plasticity and

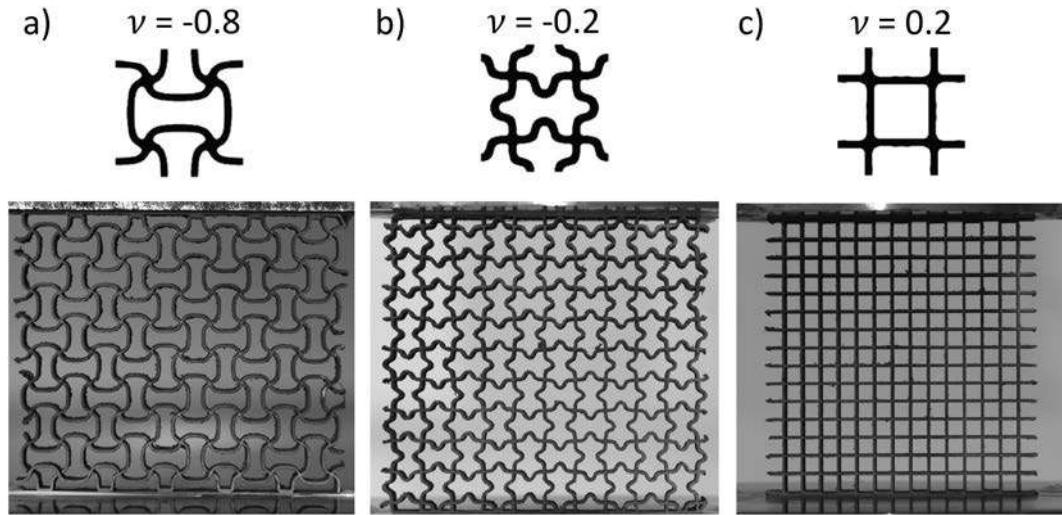


Fig. 1. Pictures of the 3 specimens manufactured by Directed Energy Deposition and tested under a compression load. Their design is originally based on an auxetic cell extracted from (Clausen et al., 2015) with a Poisson ratio of -0.8 , -0.2 and 0.2 in a), b) and c) respectively. The geometric details of the 3 fabricated specimens are available in Table 1.

Table 1
Properties the three specimens manufactured.

	$\nu = -0.8$ specimen s	$\nu = -0.2$ specimen	$\nu = 0.2$ specimen	Bulk specimen
Height (mm)	65	75	80	/
Length (mm)	71	81	74	/
Thickness (mm)	19	16	17	/
Number of cells	8×10	9×10	15×13	/
Density (kg/ m ³)	1591	1384	1588	7960

nor void nucleation neither crack propagation.

2.4. Material constitutive behavior

In order to provide data on the constitutive behavior of the manufactured wall material, a tensile test was performed on a flat dog-bone specimen. This sample was extracted from a single track-thickness wall manufactured using the same 316L powder and process parameters that have been used to fabricate the lattices. More details concerning these tests can be found in (Margerit et al., 2020). The result of the test is shown in Fig. 3. The obtained material response is characteristic of an elastic-plastic behavior and can be well reproduced using a linear hardening model with the following parameters: Young modulus $E = 200$ GPa, yield stress $\sigma_y = 500$ MPa and hardening modulus $H = 1670$ MPa. This idealized response has been used in section 5 to run numerical simulations of the full lattice specimens.

At this point, it is important to note that the intrinsic elastic-plastic behavior of the constitutive material has a consequence on the global behavior of the lattices. Indeed, the material yield stress might be reached at some locations in the structure. In the subsequent loading stages, the local material tangent stiffness would drop significantly because of the two orders of magnitude between the Young modulus E and the hardening modulus H . As a result, the lattice members that are

Table 2
Chemical properties of the 316L powder.

Elements	B	C	Mo	P	S	Ni	Fe	Mn	Cr	Si	O	N
Weight percent	<0.007	0.01	2.5	0.01	<0.01	12.2	65.36	0.4	17.3	2.1	0.002	0.08

submitted to bending rapidly convert to compliant plastic hinges as soon as the yield stress is locally reached. This particular behavior is characteristic of metallic lattices and is analyzed in more details in the following sections, where it is shown that it drives the deformation patterns.

3. Compression tests

3.1. Experimental procedure

The compression experiments for the characterization of the lattice specimen responses were performed on a MTS servo-hydraulic universal mechanical testing machine equipped with a 10 kN load cell for the specimens $\nu = -0.8$ and $\nu = -0.2$ and a 50 kN load cell for the specimen $\nu = 0.2$. The tests were performed with an engineering strain rate of $10^{-2} s^{-1}$, sufficiently low to ensure that inertial effects can be neglected. Specimens were monotonically loaded up to a target maximal strain, and then completely unloaded in order to estimate the amount of restored energy. The lateral displacement of the specimen at the end plates was unconstrained during the test. A thin sheet of PTFE was inserted between the specimen and the rig to limit the friction.

3.2. Results

An overview of the compression response of the specimens is given in Fig. 4. On the left, several snapshots are displayed corresponding to different loading stages. On the right the global response curve is plotted as the normalized load (measured load over the specimen cross-section) against the engineering strain (computed from the measured end plate displacements).

Table 3
Physical properties of the 316L powder.

Apparent density (Hall)	Flowrate (Hall)
4.2 g/cm ³	17sec/50g

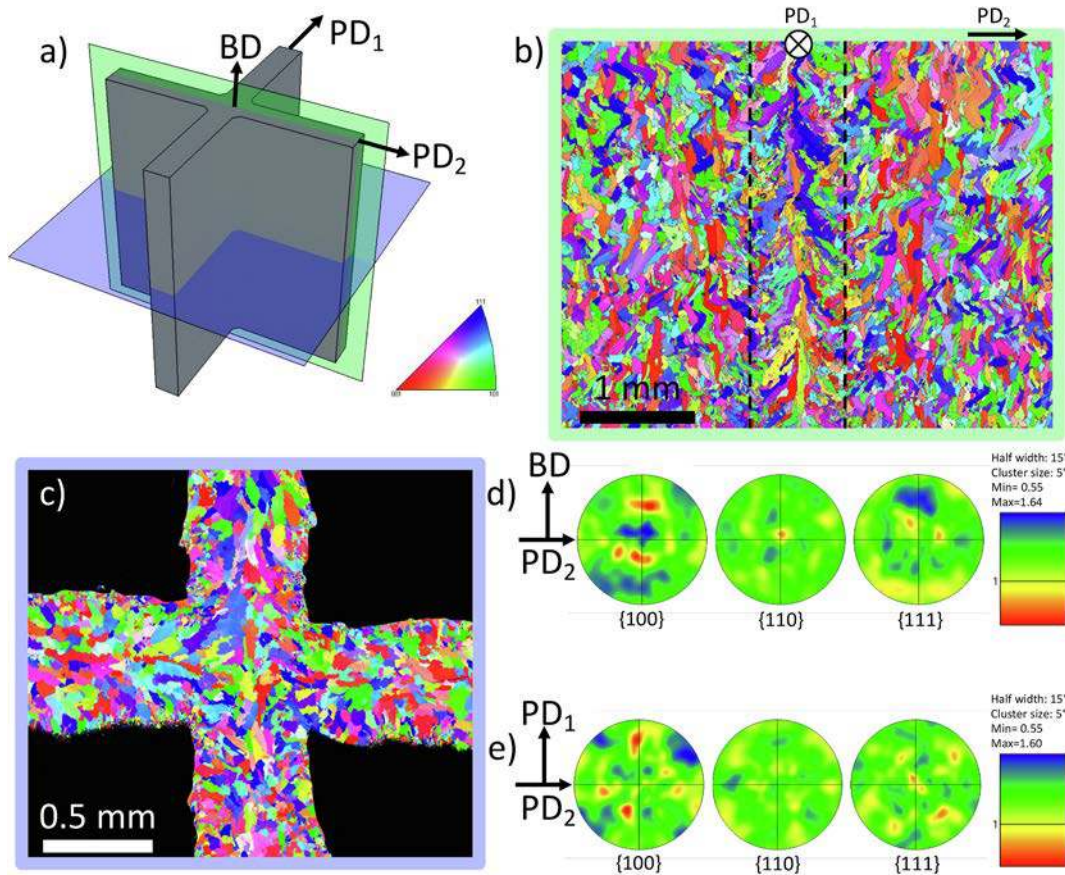


Fig. 2. Microstructure of the single-track crossing of the unit cell: (a) scheme of the crossing with building and printing direction, denoted as BD and PD respectively and planes of microscopic analysis: side and top section in green and blue respectively. b) and c) EBSD maps of the microstructure and d) e) crystallographic texture as pole Figures for the side and top section respectively. (For interpretation of the references to color in this figure legend, the reader is referred to the Web version of this article.)

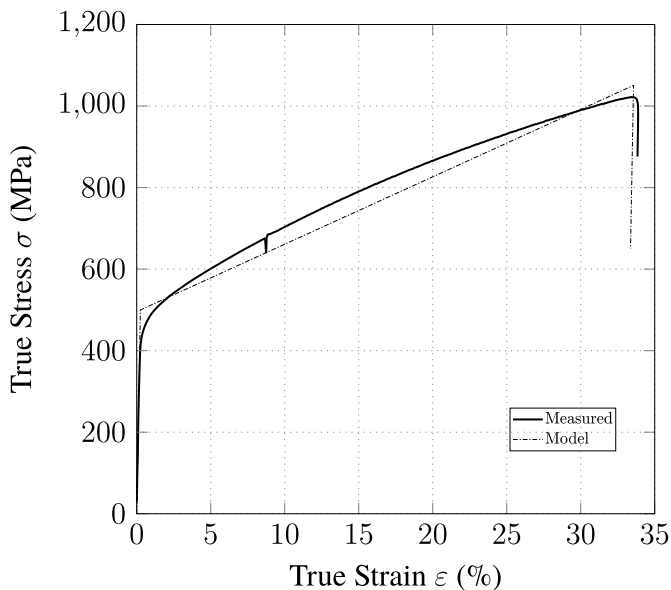


Fig. 3. Material constitutive behavior. Result of a tensile test performed on a dog-bone 316L specimen extracted from an additively manufactured wall. Measured and idealized response using a linear hardening model with Young modulus $E = 200$ GPa, yield stress $\sigma_y = 500$ MPa and hardening modulus $H = 1670$ MPa.

The observed specimen response was close to the response of foams (see (Gibson and Ashby, 1999; Gong et al., 2005) for example). Indeed, the mechanical compression behavior exhibits four characteristic zones: (i) *elastic loading* with a very steep load increasing slope; (ii) *crushing plateau* with a load being approximately constant; (iv) *densification* characterized by the increase of the measured load due to the contact between lattice members; (iv) elastic unloading.

The global engineering strain marking the transition between preceding regimes is specific for each specimen and is the consequence of both macroscopic effects (i.e. global elastic buckling) or microscopic motion (i.e. plastic localization, contact creation, member breakage). Moreover, while the load amplitude is essentially driven by the macroscopic behavior, microscopic kinematics lead to fluctuations of the load curve. As a last general remark, it can be noticed that the complete unloading always corresponds to small residual strains. Hence, only a small part of the energy is restored during the final phase, the rest being dissipated during the compression process. This effect of the lattice structure is also related to the elastic-plastic behavior of the material, i.e. the manufactured 316L, where elastic strains are also negligible in comparison with the plastic strains during the plastic flow (see Fig. 3).

The $\nu = -0.2$ specimen belongs to the class of bending-dominated lattice structures. In particular, the bending moment localizes during the early elastic stages in the central part of the vertical members where the wall is highly curved. Consequently, plastic hinges form at these points of stress localization. Hence, the global specimen compliance increases, inducing a decrease of the loading slope up to a maximal load (see Fig. 4a, stage (a)). This maximum marks also the transition to the crushing plateau characterized by a global plastic buckling mode, with a shape similar to Euler-beam buckling. As a consequence of this relative

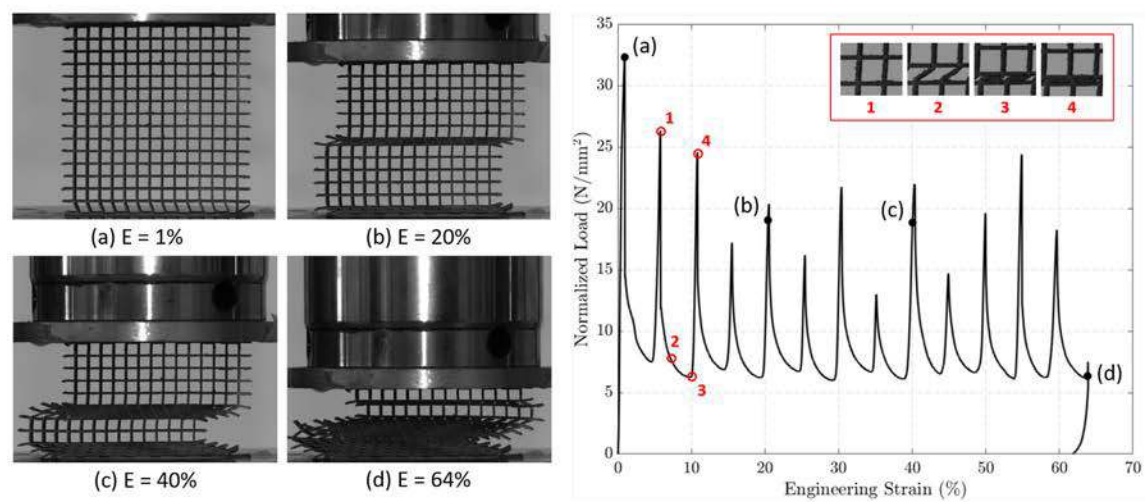
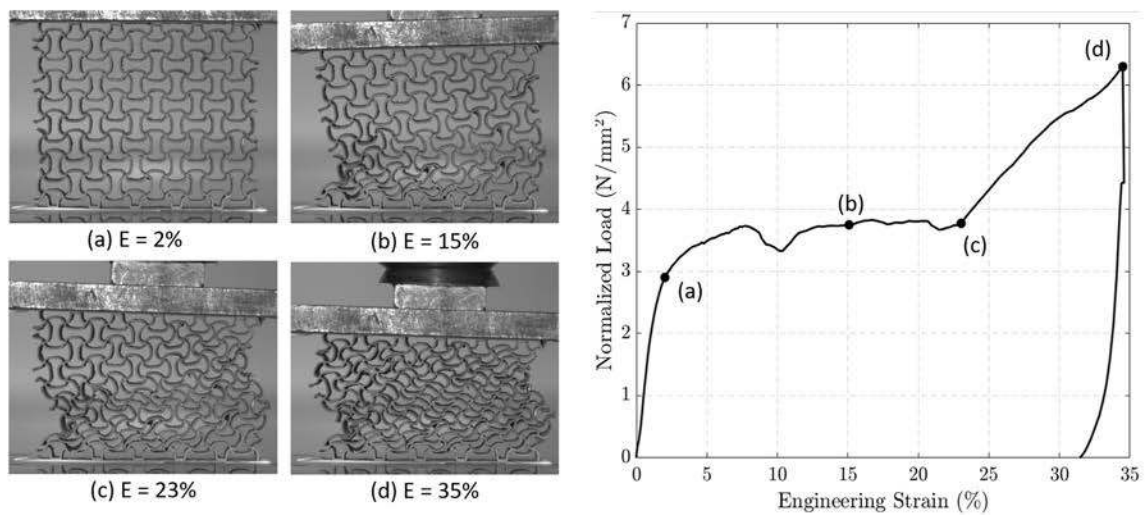
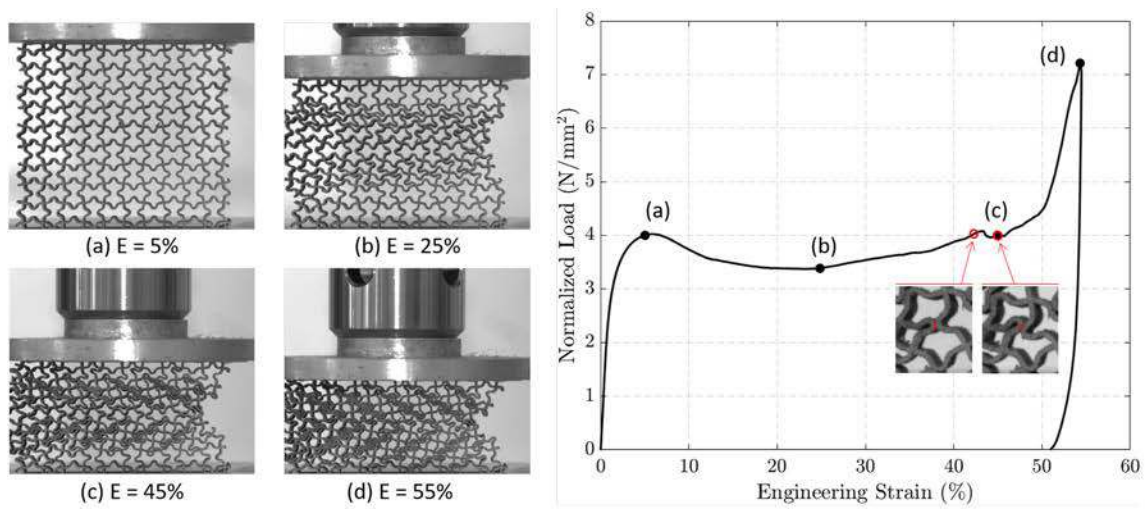


Fig. 4. Experimental compression test results. Snapshots taken for various engineering strain levels. Measured load normalized by the specimen section versus engineering strain.

instability, the load slowly decreases down to the marker (b) of Fig. 4a. Following this local load minimum, the specimen response becomes influenced by contacts occurring between the lattice members. Due to its specific unit cell geometry, the specimen folds with a highly regular herringbone pattern. This particular buckling pattern is stopped by the complete contact between adjacent walls (see marker (c) of Fig. 4a and the detail in Fig. 7a). This permits to crush the specimen up to approximately 50% engineering strain where the final densification starts. This densification regime is characterized by the cell walls being firmly in contact and exhibits a steep load increase comparable to the elastic regime one. As already mentioned, the loading curve presents several small fluctuations that are the result of microscopic motions and forces. An example is displayed on Fig. 4a around the marker (c), where a contact slip between two consecutive stages causes the load to drop. It has to be noted that the occurrence and amplitude of these fluctuations are highly sensitive to shape imperfections at the micro scale and the contact forces induced by the roughness of the wall surface.

The $\nu = -0.8$ specimen equally belongs to the class of bending-dominated structures. However, in contrast with the previous specimen, no plastic localization occurs in the early stages of the loading. Moreover, the stresses are more evenly distributed along the cell walls, as these do not present a high curvature point. An additional point concerns the relatively large number of defaults that appeared during the manufacture of the specimen, leading to incompletely fabricated walls (see Fig. 9 for details). As a consequence, the results obtained are different from the response of the pristine structure; the effect of the introduced defaults is investigated numerically in section 5. In this case, the crushing plateau starts with a slip motion due to a broken crossing at the bottom-left corner of the specimen (see Fig. 4b, snapshot (b)). This is shortly followed by contact interactions occurring at the other broken crossings which induces fluctuations of the plateau load. In this case, no clear deformation pattern could be identified during the compression, even if an horizontal shear band can be observed in the central region. This is the consequence of the unit cell geometry. More precisely, the opposite vertical walls being rather close to each other in the reference configuration, they happen to be in contact early during the compression. Consequently, the densification regime starts at approximately 25% engineering strain, see Fig. 4b, marker (c). This regime is, once again, characterized by the increasing of the surface areas in contact. However, the associated tangent stiffness increase is less marked than in the previous case. This can be explained as cells are not completely closed in this case and conduct to a lower local material density.

In contrast to the preceding lattices, the $\nu = +0.2$ specimen belongs to the category of stretch-dominated structures: in the elastic regime, the cell walls are subjected to an in-plane compression without bending. As a consequence, the transition between the elastic loading and the crushing plateau is characterized by a strong buckling instability. It is triggered at the crossings, at ends of vertical members, where plastic localizations shortly convert into hinges. These flaws propagates instantaneously to a complete row of cells, which is sheared up to its complete closing (see Fig. 4c, insets (1–4)). Subsequently, the load increases rapidly up the instability point where a new plastic hinge is created, causing the collapse of another row. Fig. 4c suggests two interpretations of the crushing response of this particular specimen: (i) considering the complete structure, with an average normalized load at approximately 10 kN/mm^2 and large fluctuations corresponding to the collapse of subsequent cell rows; or (ii) considering the structure as a stack of independent cell rows in parallel, each having its own response cycle (elastic loading, crushing and densification). Finally, one can remark that the specimens reaches a high compression strain at more than 60% engineering strain, enabled by the complete closing of the voids. The higher levels of normalized load and ultimate strains could suggest that the structure is well-suited for energy absorption. This is however not the case as high load drops associated with the full contact during the shear of the rows of cells are responsible for unwanted shocks waves which can propagate in the structure. Therefore the analysis

proposed in the following sections focuses in the two first specimens only.

As a partial conclusion, one can state that the three lattice specimen responses under compression are comparable to the response of open-cell foams, with a long crushing plateau followed by a densification phase. The deformation pattern is governed by microscopic features corresponding to the cell geometry as well as the formation of plastic hinges and the failures of crossings and walls.

4. Kinematic analysis

The observation of the specimen responses shows that the lattice behavior is determined by its kinematics: (i) at the scale of the unit cell (macroscopic scale), where effective properties can be considered, and (ii) at the microscopic scale, where the material constitutive behavior is at play. In this section, we use an adapted Digital Image Correlation procedure to follow geometrical features of the lattice in order to provide quantitative results on the multi-scale kinematics of the specimen. In particular, we focus on (i) the characterization of the deformations of unit cells (see Fig. 7) and (ii) on the rotation of walls at crossings (see Fig. 8), driven by the formation of plastic hinges, which reveal the deformation patterns of the lattice.

4.1. DIC procedure

For the needs of the study, an adapted Digital Image Correlation (DIC) procedure has been implemented based on an academic code written in MATLAB. This procedure uses local imaget-based DIC. The main assumption states that the relative transformation between sub-domains of two subsequent images of the test is a uniform translation. In order to reduce the influence of the displacement gradient in the tracking of geometrical features, small subdomains are used; large rotations occurring in the lattice are computed from the relative displacement between two subsequent stages. The procedure is illustrated in Fig. 5, where an inset of a lattice is shown. Tracked points are associated with the image sub-domains highlighted with solid lines.

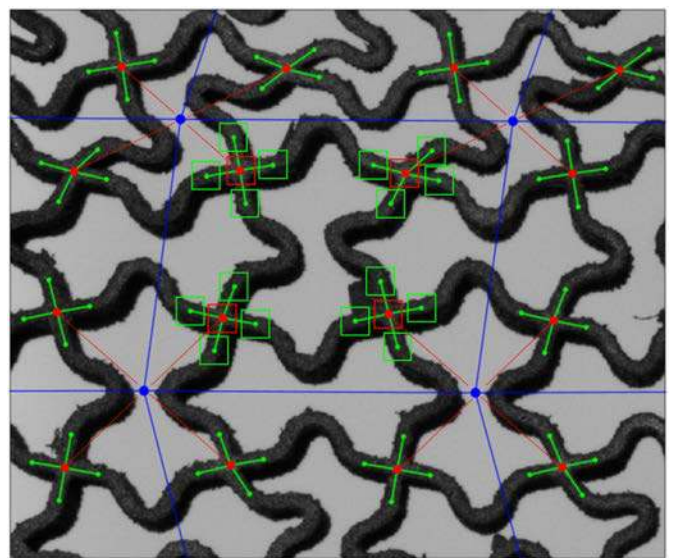


Fig. 5. Geometry tracking using Local Digital Image Correlation. Procedure: (1) tracking of the physical nodes (red dots); (2) following of the adjacent members (green dots and edges); (3) computation of the virtual unit cell corner positions (blue markers) as the middle point between adjacent nodes. The deformed unit cell geometry is denoted by blue lines. Red/green squares denote the image sub-domains used to perform DIC. (For interpretation of the references to color in this figure legend, the reader is referred to the Web version of this article.)

4.2. Unit cell kinematics

As the corners of the unit cells are not attached to any *material* point of the lattice (see blue markers in Fig. 5), they cannot be directly tracked using DIC. However, it is possible to define a *virtual* corner of the cell, as the average of the positions of the four neighboring crossings (see red dashed lines in Fig. 5). This operation permits to reconstruct the unit cell (blue quadrilateral) and to deduce its macroscopic deformations, as the average strains in each unit cell (see (Allais et al., 1994; Balit et al., 2020a) for details).

The procedure can be summarized in the following steps: (i) tracking of the material nodes at the center points of each crossing (red dots), (ii) computation of the unit cell kinematics (in blue), (iii) computation of the positions of the members of the crossings (in green). In order to illustrate the procedure, an animation of the obtained macroscopic deformations is included in the supplementary materials (see *m02_UnitCellStrains.mp4*). The kinematics of the unit cells of the two specimens are summarized in Fig. 6, where the transverse engineering strain E_{11} is plotted as a function of the longitudinal compression engineering strain E_{22} . For the sake of readability, unit cells have been clustered and colored to separate different behaviors. In addition, the theoretical (as-designed) Poisson ratio corresponding to each specimen is shown with a dashed black line.

The response of the unit cells of the $\nu = -0.2$ specimen shown in Fig. 6a, can be separated into two regimes: (i) a linear response followed by (ii) a nearly constant transverse strain. The transition between the two phases is governed by the onset of shear in each cell, mainly due to the nature of the Euler-beam-like buckling mode. It can be observed that the cells in the central region follow the theoretical Poisson ratio in the linear regime. Cells colored in purple behave linearly up to 15% engineering strain. These cells are located around the inflexion point of the global buckling mode (see Fig. 4a, snapshot (b)) and are thus mostly transversely loaded. In contrast, the boundary cells located at the top and bottom rows and colored in red and blue respectively in Fig. 6a, are rapidly submitted to shear. Their transverse motion (E_{11}) is constrained by the specimen's end plates, and consequently, generate a different response than the theoretical behavior associated with an homogeneous transverse strain field assumption.

The kinematics of the $\nu = -0.8$ specimen is highly influenced by the failure of a number of its walls and crossings associated with a number of flaws that propagated during the fabrication. As a consequence, the

obtained macroscopic strain field is highly heterogeneous, as illustrated in Fig. 6b. Despite this high heterogeneity, two observations made on the previous specimen can be retrieved: (i) the central cell behavior (cell 5 in blue) is close to the theoretical Poisson ratio in the early stages; (ii) the cells close to boundaries (in purple) are less submitted to transverse strain. As mentioned above, the onset of crushing of the specimen is accompanied by a transition of the macroscopic cell's strain response from transverse-dominated to shear-dominated. As a consequence of the relatively long phase associated with the specimen crushing (by comparison to the elastic loading phase), the transverse strains remain fairly low all along the specimen loading, in comparison to shear strains ($E_{12}^{\max}/E_{11}^{\max} \approx 5$ and 2.5 for the specimens $\nu = -0.2$ and $\nu = -0.8$ respectively).

4.3. Rotation and flattening of the crossings

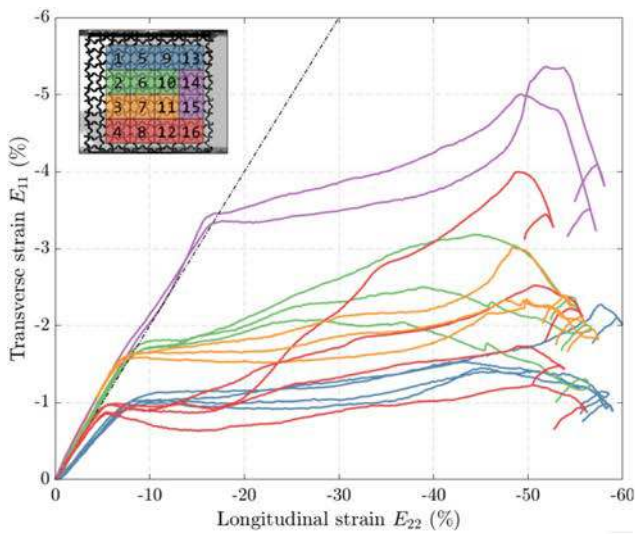
Once the macroscopic strains have been retrieved, the crossing arms are tracked in order to relate the deformation of the crossing to the corresponding unit cell strains. This is performed by defining nodes at a fixed distance from center point of each crossing. The arms are therefore defined by four additional points as suggested by the green features in Fig. 5. These new material points are then tracked using local DIC in order to provide information on the deformation of each crossing during the test. In order to illustrate the results, animations of the tracking of the crossings of both specimens are included in the supplementary materials (see *m02_CrossRotation.mp4* and *m08_CrossRotation.mp4*).

The rotation of the arms of the crossings are denoted by the angles $\theta_m^c(t)$, with $m = 1, \dots, 4$, where m and c respectively denote the index of the arms and the crossing. From the computed data set, we propose here to analyze the global rotation and the flattening deformation of each crossing, respectively described by the average rotation of each crossing $\mu^c(t)$ and its absolute deviation $\sigma_c(t)$. They are defined as follows:

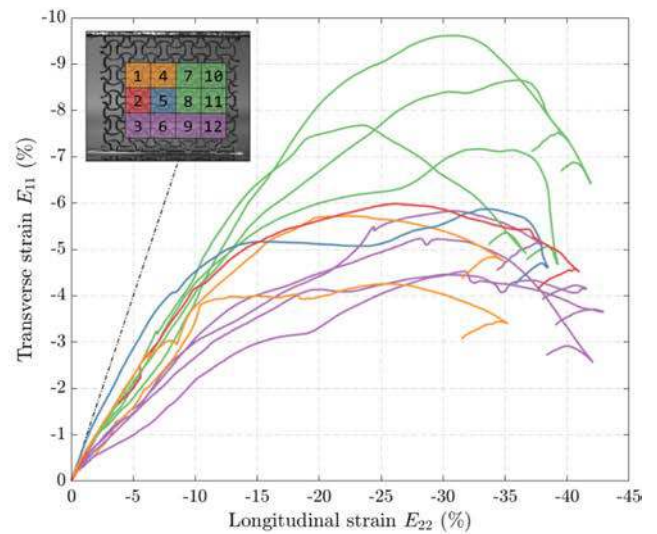
$$\mu^c(t) = \frac{1}{4} \sum_{m=1}^4 \theta_m^c(t) \quad (4.1)$$

$$\sigma_c(t) = \frac{1}{4} \sum_{m=1}^4 |\theta_m^c(t) - \mu^c(t)| \quad (4.2)$$

The results of the analysis applied to the two lattices of interest are illustrated in Fig. 7. For each specimen, the rotation and flattening

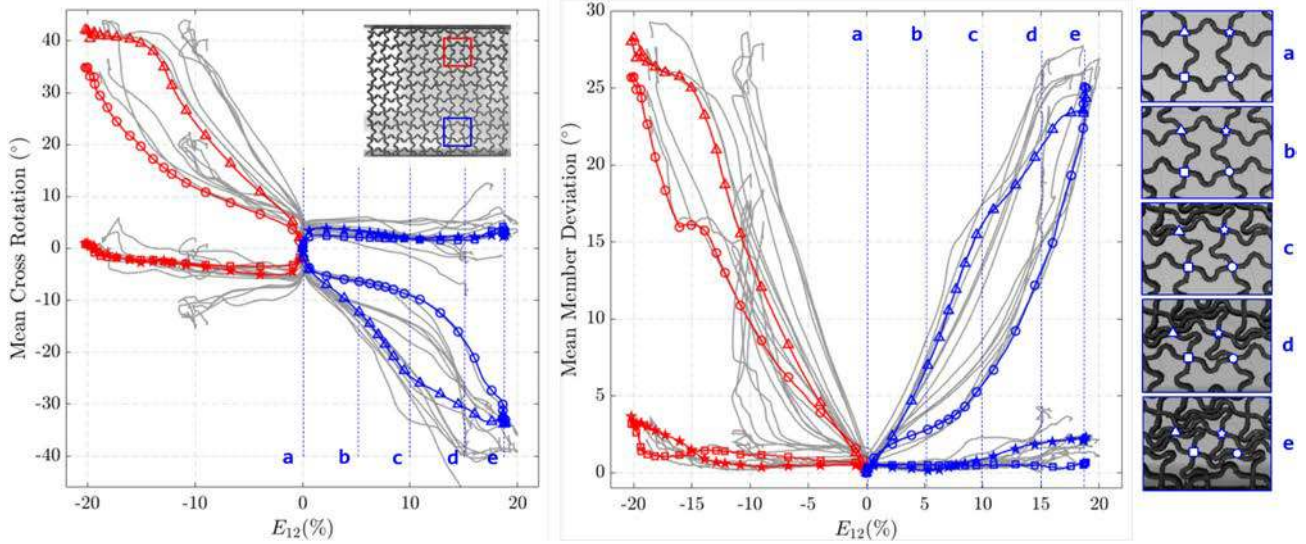


(a) Specimen $\nu = -0.2$.

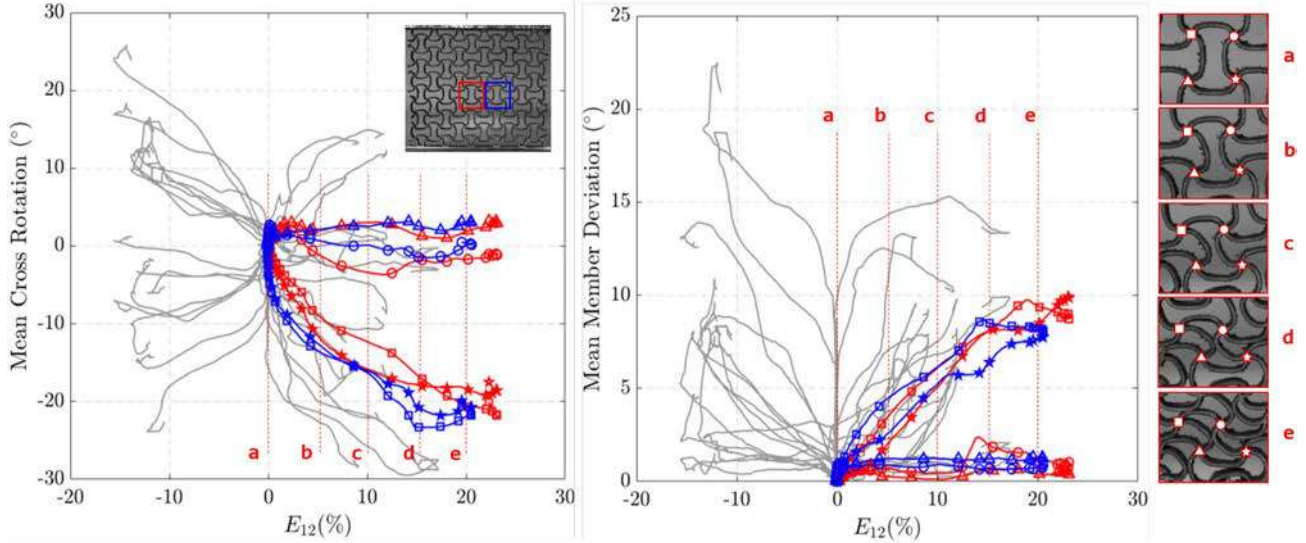


(b) Specimen $\nu = -0.8$.

Fig. 6. Unit cell strain history. Transverse strain versus longitudinal (compression) strain at the level of each individual unit cells. Colors correspond to identified cell clusters as shown in insets. (For interpretation of the references to color in this figure legend, the reader is referred to the Web version of this article.)



(a) Specimen $\nu = -0.2$.



(b) Specimen $\nu = -0.8$.

Fig. 7. Cross rotation with respect to the unit cell shear strain. (a) mean cross rotation μ^c (eq. (4.1)); (b) mean member absolute deviation σ^c (eq. (4.2)); (c) inset following a particular cell. Individual crossings belonging to this unit cell are denoted by different marker shapes.

behaviors have been plotted in gray for all the crossing in order to identify and separate the different clusters. In addition, for both specimens, two interesting cells have been highlighted in red and blue, allowing a better representation of the rotation and flattening taking place in the structure. Finally, a close view of one cell for each specimen has been added for different loading stages and enable a finer understanding. More specifically, each crossing of the cell has been associated with a different marker (round, square, triangle and star). The data corresponding to labeled crossings at different loading stages can be retrieved on their respective curves.

As mentioned in the preceding paragraphs, unit cells of both specimen are mainly submitted to shear during the crushing plateau, i.e., the phase where most of deformation take place in the crossings. In order to take an insight in the deformation mechanism, the next plots will exhibit the mean rotation and deviation of the crossings as a function of the corresponding unit cell shear strain E_{12} .

Crossing deformations are closely related to plastic hinge formation and rotations. As a consequence, two cases can be distinguished in the results: (i) plastic localization is formed at a crossing, which become

plastic hinges with low stiffness and huge deformations, (ii) crossings do not localize deformation therefore keep their original stiffness and shape. In the latter case, crossings have only small rotations during the loading. Indeed, if crossings turn, they cause large motions in the neighboring cells. The two cases can be clearly observed in the data presented in Fig. 7, where two types of curves can be seen: (i) highly flattened crossings with large values for both the mean rotation μ^c and deviation σ^c (specimen $\nu = -0.2$, triangle and round markers and specimen $\nu = -0.8$, square and star markers), (ii) undeformed crossings, characterized by the vanishing of μ^c and σ^c (specimen $\nu = -0.2$, square and star markers and specimen $\nu = -0.8$, triangle and round markers).

For the $\nu = -0.2$ specimen, two cells located symmetrically with respect to the mean horizontal axis of the structure are highlighted in red and blue in Fig. 7a. This enables to observe a symmetric behavior of the crossing deformation as well as a clear and highly repeatable deformation pattern when looking at the complete data set represented by the gray curves. One can remark the presence of curve clusters composed of crossings opposed to the highlighted cells remaining undeformed while the two other ones are highly flattened. In addition, one can notice that

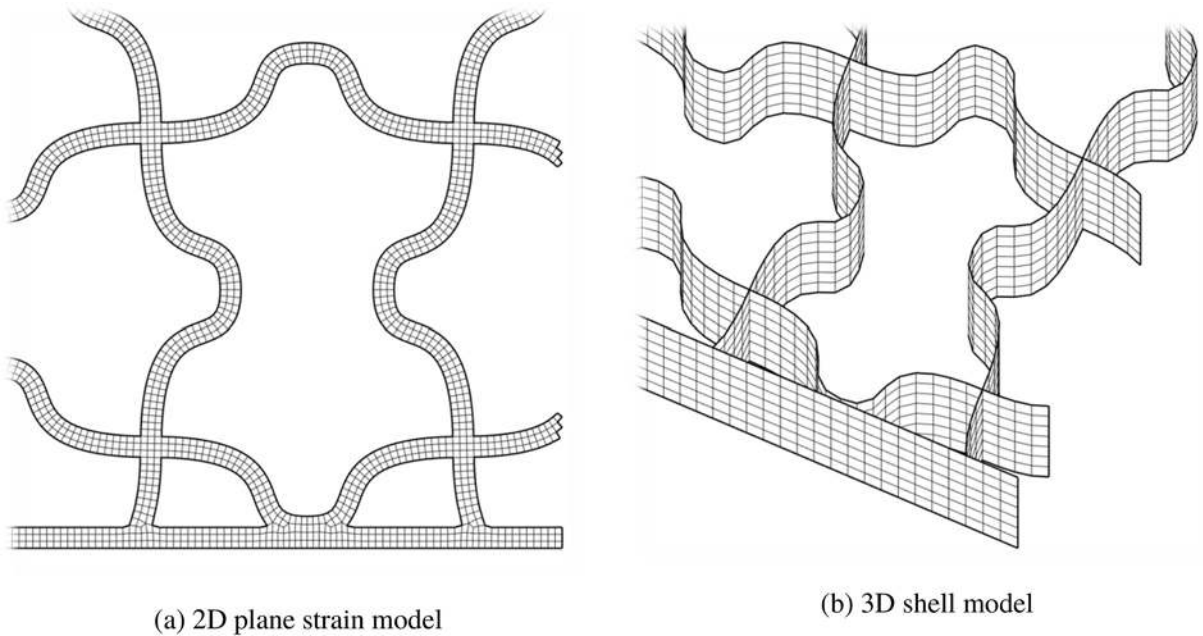


Fig. 8. View of the meshes built to perform the finite element simulations of the lattices crushing tests.

while the data corresponding to the two deformed crossings (round and triangle markers) are close to each other, a noticeable difference can be seen around the stage (c); this is directly related to the heterogeneity of the macroscopic strain field at this location close to the specimen boundaries. This last observation clearly shows an effect of the macroscopic strain gradient in the microscopic deformation of the specimen, highlighting the need of refined homogenization theories in order to sample correctly the structure’s homogenized properties.

Once again, the highly heterogeneous macroscopic strain field that characterizes the $\nu = -0.8$ specimen, consequence of the presence of a number of broken walls, makes the data less regular. However, the central row of cells appears to be nearly uniformly sheared during the test. The behavior of two cells located in this row are presented in red and blue in Fig. 7b. For this configuration, the shear strain is fairly uniform in this region, resulting in the vanishing of the strain gradient. Hence, no noticeable difference is observed between the mean rotation and deviation data corresponding to deformed crossings.

5. Numerical simulations

This last section presents the numerical simulations of the compression tests. We show that the numerical response matches the experimental observation, allowing to study its sensitivity with respect to modeling assumptions (3D shell plane stresses, 2D plane strains, strain rate), geometrical parameters (wall thickness, cell geometry) or defaults (wall breakages).

5.1. Model definition

The numerical models are implemented in the commercial Finite-Element solver Abaqus/Explicit. Explicit solvers have the ability to accommodate numerous surface-to-surface contacts as well as structural instabilities without the introduction of a geometrical imperfection. Pure quadrilateral finite element meshes are generated using MATLAB scripts by starting from a wire-frame definition of the unit cell geometry (wall medial axis). The mesh generation procedure results with two type of meshes presented in Fig. 8 as 2D plane-strain “CPE4” and 3D plane-stress shell “CPS8” elements in a) and b) respectively. The 2D elements are preferred to model contacts. They allow a proper definition of the outer surfaces of the specimen which are likely to be in interaction.

However, a reasonable discretization of the wall thickness by a minimum number of elements is needed for the 2D formulation, thus increasing the computational cost as the stable time increment is directly related to the element size in explicit solvers. In contrast, the 3D shell model directly takes into account the wall thickness in the element computation, by integrating the trough-the-thickness strain and stress distributions directly in the element behavior. In addition, the variation of mechanical fields along the third direction (direction of extrusion) is taken into account, that can be used to validate the plane strain assumption of the 2D model. However, the shell integration imposes the reduction of the self-contact thickness in the neighborhood of crossings in order to avoid spurious reactions, thus providing a poor description of the contact surfaces in the densification regime.

An elastic-plastic constitutive behavior for the manufactured material with a linear hardening law sampled on the tensile behavior (see Sec. 2.4 and Fig. 3) is defined for the manufactured material. The contact law is Kinematic hard contact, with no tangent friction.

5.2. Results and comparisons

The comparison of various numerical simulations with the experimental curves are illustrated in Fig. 9.

The objective here is, for the $\nu = -0.2$ specimen, to evaluate the effects of the model parameters on the results: modeling assumptions, wall thickness and applied strain rate. Results are summarized in Fig. 9, where the geometry of the specimen at the maximum strain stage has been added for the 3D shell model and the 2D plane-strain model. Computations provided an excellent prediction of the elastoplastic buckling mode and densification pattern for both lattices when compared with snapshot (d) of Fig. 4a. For a fixed 0.6 mm wall thickness (dimension measured by caliper on the wall), two different simulations were run for the 3D model using a strain rate of $0.6s^{-1}$ and $1s^{-1}$ plotted in dashed green and orange respectively, see Fig. 9a.

While the computed response is fairly identical at the early stages, a noticeable difference appears in the densification regime. Inertia effects combined with contact reactions tends to overestimate the specimen normalized load at higher strain rates. For the same thickness and a lower strain rate, the 2D model exhibits similar load levels when compared to the 3D model. However, during the densification phase the occurring hard contacts result in higher reactions. With regard to

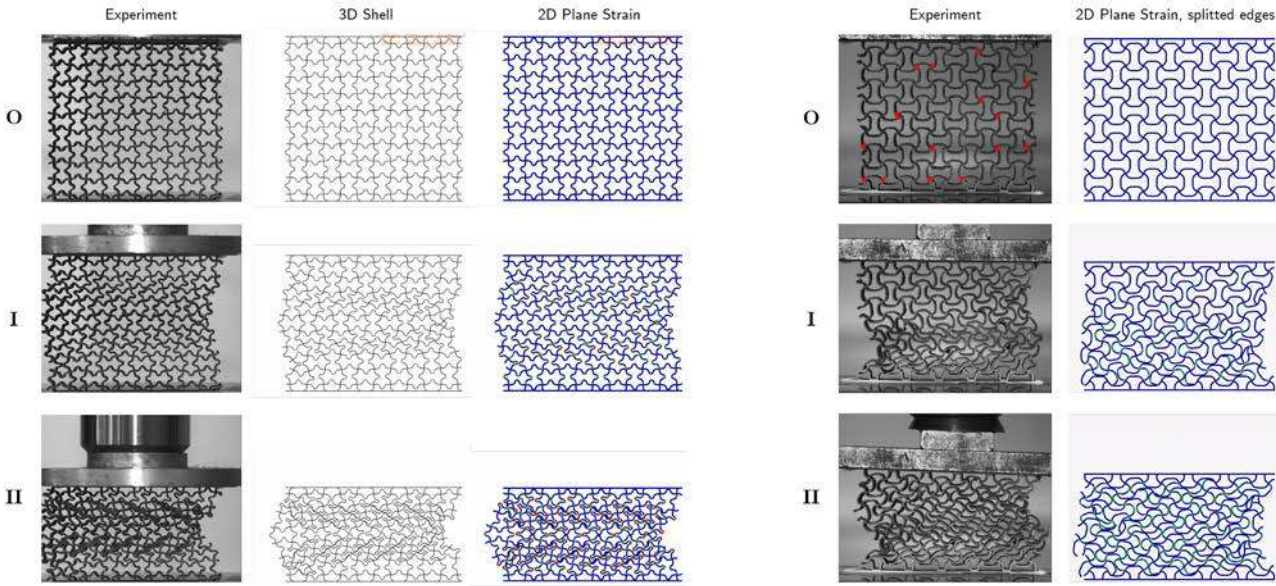
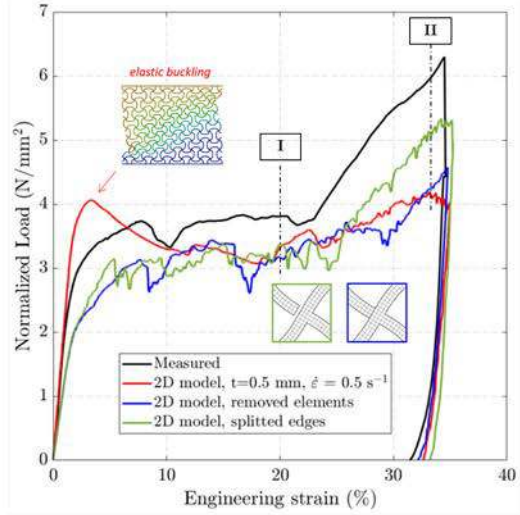
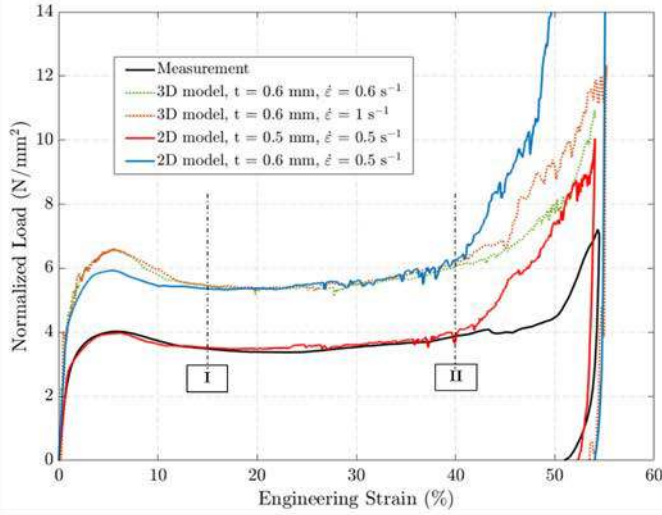


Fig. 9. Comparison between measured and simulated structural responses for both specimens.

experimental results (see the black curve), the two different modeling assumptions provided a coherent response, even if the global load values seems overestimated. By reducing the theoretical wall thickness down to 0.5 mm, an excellent match with the experimental load levels was found. This reduction of the wall thickness can be justified by the high surface roughness and waviness of the lattices walls (Margerit et al., 2020), that can easily be observed on the EBSD in Fig. 2; it is indeed expected to drastically reduce the bending stiffness of the wall. The stiffening after the densification point is nonetheless higher in the simulations than in experiments. This gap could have been reduced by introducing a softer contact law in the model. With the chosen geometrical parameters, the kinematics of the structure observed in the experiments is well reproduced by the model. To illustrate this point, an animation of both experimental and numerical results is provided as supplementary material (see *m02_Comparison_t05.mp4*).

For the $\nu = -0.8$ specimen, the computations were directly performed with the optimal parameters found previously (wall thickness and strain rate). The purpose of the computations concerning this specimen is to evaluate the consequence of defects (i.e. wall and crossing failures) on the global behavior of the specimen. The results are summarized in Fig. 9, where an image of the lattice have been added, with lines denoting broken wall locations on the tested specimen. First, a 2D

simulation was run on the pristine structure, with no failures (red curve). One can remark that while the measured elastic loading is well sampled by the model, a global elastic buckling mode is observed, associated with a higher load at the start of the crushing plateau. This response highlights that defects accelerate the onset of the specimen crushing. Next, the defects of walls and crossings are introduced in the model, at the exact locations where broken walls have been identified in the tested specimen. These defects are introduced using two strategies: (i) element removal or (ii) edge splitting. The first solution creates a gap with a size depending on the local element size, while the second method create an infinitely thin slit. Observing the corresponding results in Fig. 9, one can see that difference are mainly noticeable in the densification phase. Indeed, flaws introduced by edge splitting are more rapidly closed, thus causing higher reaction forces. Finally, one can state that the introduction of defects, as crossing failures, improves the results as the onset of crushing is better sampled by the modified model.

6. Conclusion

The present work proposed an analysis of 2D extruded lattice structures manufactured by Directed Energy Deposition. The metallurgical state of the specimens as well as their mechanical properties were

investigated at different scales. The results show that the process produces a sound microstructure, leading to an elasto-plastic constitutive behavior weakly influenced by the laser scanning strategy. The experimental compression tests have shown that the lattices exhibit a foam-like behavior at the global scale, characterized by an elastic loading, a crushing plateau and a final densification regime. At the end of the test, the presence of the plateau and the small residual strains associated with specimen unloading have shown the high energy absorption capabilities of the specimens. Moreover, it was noticed that depending on the unit cell design, a clear buckling mode could be observed and associated with a particular pattern of macroscopic strains, cell wall contacts and crossing deformations.

The on-purpose developed DIC procedure allowed to precisely analyze the kinematics of the structure under compression, by tracking the strain behavior of individual unit cells and deformation of the wall crossings. Furthermore, the ability to extract local data at several branches and crossings of the lattice was used to provide statistical characterization of the lattice behavior as well as a more precise understanding of the buckling pattern.

Companion numerical computations were presented, implementing two different models: using 2D plane strain elements or 3D shell elements. Both models successfully predicted the compression behavior in terms of elastic moduli, crushing plateau and the beginning of the densification regime. The level of the crushing plateau showed to be dependent on the thickness of the branches of the lattice and the friction due to self-contacts occurring in each cell. Both parameters are a function of the surface roughness of the lattice walls resulting from the DED process. As a consequence, they are highly dependent on the chosen process parameters, and their calibration represents an interesting perspective of work.

In this work, it was shown that metallic lattice structures have a good energy absorption capacity up to 50% compressive strain and a global

strengthening in the densification zone. Due to its ability to print on non-planar substrates, the DED process can thus be considered as a good candidate technology to add energy absorption capacities to various structures.

Credit author statement

Yanis Balit: Conceptualization, Methodology, Investigation, Writing. Pierre Margerit: Conceptualization, Methodology, Investigation, Writing. Eric Charkaluk: Conceptualization, Editing & Reviewing. Andrei Constantinescu: Conceptualization, Editing & Reviewing.

Declaration of competing interest

Crushing of additively manufactured thin-walled metallic lattices: two-scale strain localization analysis The authors whose names are listed immediately below certify that they have NO affiliations with or involvement in any organization or entity with any financial interest (such as honoraria; educational grants; participation in speakers' bureaus; membership, employment, consultancies, stock ownership, or other equity interest; and expert testimony or patent-licensing arrangements), or non-financial interest (such as personal or professional relationships, affiliations, knowledge or beliefs) in the subject matter or materials discussed in this manuscript.

Acknowledgments

The authors would like to thank the *Direction Générale de l'Armement* (DGA) and the *Société Nationale des Chemins de fer Français* (SNCF) for providing the funding. The authors would also like to acknowledge Sylvain Durbecq, Alexandre Tanguy and Simon Hallais for accompanying the fabrication of specimens and SEM measurements.

Appendix A. Detailed microstructure analysis

In order to obtain the study the local microstructure at the intersection between lattice walls (see Fig. 3), a crossing was extracted from the manufactured structure. It was mechanically polished with silicon carbide abrasive papers with successive grit values from 400 to 4000 and finished with a 1 μm diamond paste until a mirror surface was obtained. The specimens were finally ion polished during 1 h in a PECS II machine from Gatan (Oerlikon) using the following parameters: 6° polishing angle, 6 keV electron beam power, 6 rpm specimen angular velocity. The microstructure of the specimens was examined by an Electron Backscatter Diffraction (EBSD) technique on a FEI QUANTA 600F Scanning Electron Microscopy (SEM) apparatus. Data was collected and analyzed using the Aztec and Channel 5 software respectively. For both view planes, the EBSD were collected with a step size of 1 μm ; results are presented in Fig. 3.

The EBSD map on the side plane presents two distinct patterns of microstructure which stand for the two tracks with printing directions PD_1 and PD_2 (see Fig. 3b). Both microstructure patterns exhibit grains with an ellipsoidal shape. The central region of the side plane corresponds to the crossing of the two tracks and between the dashed lines, a fir tree arrangement of the grains is present. This pattern is equally observable at the sections of single track walls as shown in (Balit et al., 2020b; Guévenoux et al., 2020). Thus, this specific microstructure denotes that the transverse printing direction PD_1 is controlling the crystallization in this region. Moreover, the particular fir tree pattern is the result of two competitive heat dissipation mechanisms (Guévenoux et al., 2020): (i) heat flow through diffusion in the wall through the previously deposited layers and (ii) heat convection at the outer surfaces. Outside the central region, we recover the herringbone pattern of single track walls with printing direction PD_2 . This noticeable pattern is a consequence of the alternating movement of the laser head during the manufacturing, which controls the local thermal history and the direction of maximum heat flow in different layers (see (Balit et al., 2020a; Guévenoux et al., 2020) for more details). The EBSD map of the top section displayed in Fig. 3c exhibits the epitaxial growth of several grains between the two regions.

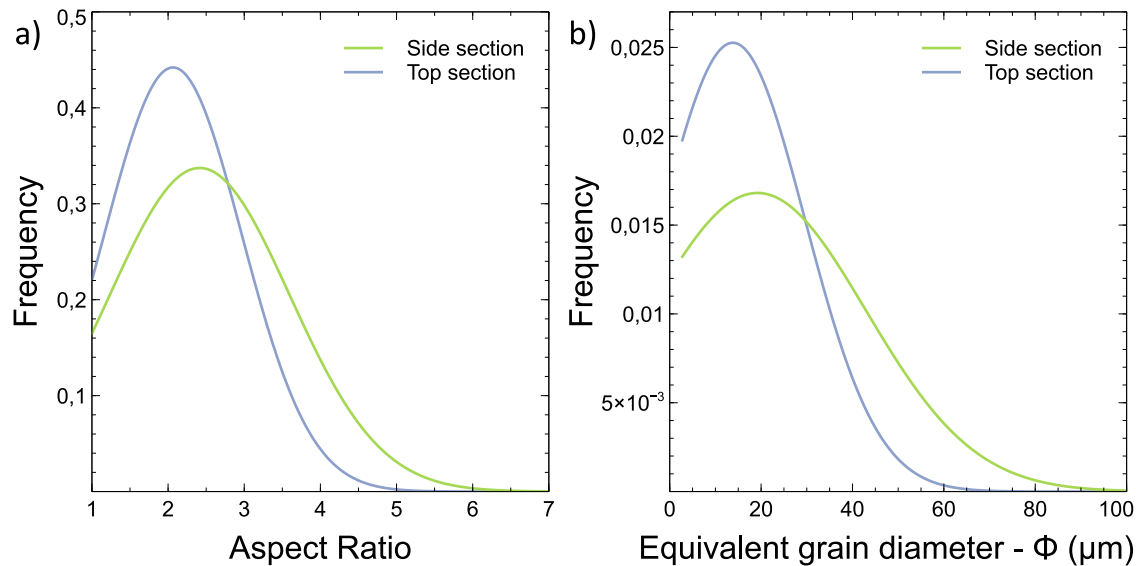


Fig. A.10. Probability density functions for the grain parameters: a) shape expressed as an aspect ratio of the equivalent ellipse and b) grain size expressed as the equivalent grain diameter.

The grain morphology was statistically analyzed from the EBSD maps. The shape and size of individual grains is described by: (i) the equivalent grain diameter defined as the diameter of a disk with a surface equal to the grain area and (ii) the aspect ratio which corresponds to the ratio of the principal axes of the smallest circumscribed ellipse. Results are summarized in Fig. A.10; the distribution corresponding to the side and top plane are defined by the green and blue curves respectively. The average aspect ratio of grains in the top section is equal to 2.06, with a standard deviation of 0.9, whether it reaches 2.42, with a standard deviation of 1.18 for the side section. This indicates that the grains present a more columnar morphology with respect to the side section when compared to the top one.

The crystallographic texture obtained from the EBSD data was plotted for the side and top views in Fig. 3d and e respectively. Three inverse pole figures, computed with respect to the crystallographic planes {100}, {110} and {111}, are displayed for both sections. One can observe that for both figures that the texture level is relatively moderate, 1.64 and 1.60 in Fig. 3d and e respectively, as well as a more dominant and preferred orientation for the planes {100}. The crystallographic texture in an additively manufactured part is usually associated with the thermal gradient flow and the intrinsic crystalline structure of the material. The material used in this study, 316L stainless steel, is a face-centered cubic crystal which usually exhibits a grain growth occurring along the <100> crystallographic direction as the crystallographic plan {100} is the least dense atomic plan. Therefore, a particular crystallographic texture pattern is often observed in the literature (Balit et al., 2020a, 2020b) due to fact that, during the solidification, the grains with the <100> direction are aligned with the maximum thermal gradient. It is notably illustrated for a FCC structure in (Guévenoux et al., 2020) where the effect of the dwell time between successive layers on the crystallographic texture and the morphology of the grains was investigated. In this study, no clear pattern of crystallographic texture could be highlighted as one can see in Fig. 3d and e.

References

- Abe, Takeyuki, Sasahara, Hiroyuki, August 2019. Layer geometry control for the fabrication of lattice structures by wire and arc additive manufacturing. *Additive Manufacturing* 28, 639–648.
- Agnelli, Filippo, Constantinescu, Andrei, Nika, Grigor, 2020a. Design and testing of 3d-printed micro-architected polymer materials exhibiting a negative Poisson's ratio. *Continuum Mech. Therm.* 32 (2), 433–449.
- Agnelli, Filippo, Margerit, Pierre, Celli, Paolo, Daraio, Chiara, Constantinescu, Andrei, 2020b. Systematic two-scale image analysis of extreme deformations in soft architected sheets. *Int. J. Mech. Sci.* 106205.
- Allaire, Grégoire, 2012. *Shape Optimization by the Homogenization Method*, vol. 146. Springer Science & Business Media.
- Allais, L., Bornert, M., Bretheau, T., Caldemaison, D., 1994. Experimental characterization of the local strain field in a heterogeneous elastoplastic material. *Acta Metall. Mater.* 42 (11), 3865–3880.
- Antolak-Dudka, Anna, Platek, Pawel, Durejko, Tomasz, Baranowski, Pawel, Malachowski, Jerzy, Sarzynski, Marcin, Sarzynski, Sarzy, Czujko, Tomasz, 2019. Static and dynamic loading behavior of ti6al4v honeycomb structures manufactured by laser engineered net shaping (lens tm) technology. *Materials* 12 (1–20).
- Ashby, Michael F., 2006. The properties of foams and lattices. *Phil. Trans. Math. Phys. Eng. Sci.* 364 (1838), 15–30.
- Balit, Yanis, Charkaluk, Eric, Constantinescu, Andrei, 2020a. Digital image correlation for microstructural analysis of deformation pattern in additively manufactured 316l thin walls. *Additive Manufacturing* 31, 100862.
- Balit, Yanis, Guévenoux, Camille, Alexandre, Tanguy, Upadhyay, Manas V., Charkaluk, Eric, Constantinescu, Andrei, 2020b. High resolution digital image correlation for microstructural strain analysis of a stainless steel repaired by directed energy deposition. *Mater. Lett.* 270, 127632.
- Baranowski, Pawel, Platek, Pawel, Antolak-Dudka, Anna, Sarzynski, Marcin, Kućwicz, Michał, Durejko, Tomasz, Malachowski, Jerzy, Janiszewski, Jacek, Czujko, Tomasz, 2019. Deformation of honeycomb cellular structures manufactured with laser engineered net shaping (lens) technology under quasi-static loading: experimental testing and simulation. *Additive Manufacturing* 25, 307–316. www.beam-machines.com.
- Bradley, Hanks, Joseph, Berthel, Frecker, Mary, Simpson, Timothy W., 2020. Mechanical properties of additively manufactured metal lattice structures: data review and design interface. *Additive Manufacturing* 35, 101301.
- Chen, Yi, Zhao, Binghao, Liu, Xiaoning, Hu, Gengkai, 2020. Highly anisotropic hexagonal lattice material for low frequency water sound insulation. *Extreme Mechanics Letters* 40, 100916.
- Clausen, Anders, Wang, Fengwen, Jensen, Jakob, Sigmund, Ole, Lewis, Jennifer, 2015. Topology optimized architectures with programmable Poisson's ratio over large deformations. *Adv. Mater.*
- Dassonville, Thibault, Poncelet, Martin, Auffray, Nicolas, 2020. Toward a homogenizing machine. *Int. J. Solid Struct.* 191–192, 534–549.
- Dheyaa, S.J. Al-Saedi, Masood, S.H., Muhammad, Faizan-Ur-Rab, Alomarrah, Amer, Ponnusamy, P., 2018. Mechanical properties and energy absorption capability of functionally graded f2bcc lattice fabricated by slm. *Mater. Des.* 144, 32–44.
- Emmanuel Viard, Antoine, Dirrenberger, Justin, Forest, Samuel, 2020. Propagating material instabilities in planar architected materials. *Int. J. Solid Struct.* 202, 532–551.
- Gibson, Lorna J., Ashby, Michael F., 1999. *Cellular Solids: Structure and Properties*. Cambridge university press.
- Gong, L., Kyriakides, S., Triantafyllidis, N., 2005. On the stability of kelvin cell foams under compressive loads. *J. Mech. Phys. Solid.* 53 (4), 771–794.
- Gu, Huaiyuan, Pavier, Martyn, Shterenlikht, Anton, 2018. Experimental study of modulus, strength and toughness of 2D triangular lattices. *Int. J. Solid Struct.* 152–153, 207–216.
- Guévenoux, Camille, Hallais, Simon, Charles, Alexandre, Charkaluk, Eric, Constantinescu, Andrei, 2020. Influence of interlayer dwell time on the

- microstructure of inconel 718 laser clad components. *Opt Laser. Technol.* 128, 106218.
- Harris, J.A., McShane, G.J., 2020. Metallic stacked origami cellular materials: additive manufacturing, properties, and modelling. *Int. J. Solid Struct.* 185–186, 448–466. <https://www.oerlikon.com/metco>. <https://www.oerlikon.com/metco>.
- Hutchinson, Robert G., Fleck, Norman A., 2006. The structural performance of the periodic truss. *J. Mech. Phys. Solid.* 54 (4), 756–782.
- Leary, Martin, Mazur, Maciej, Elambasseril, Joe, McMillan, Matthew, Chirent, Thomas, Sun, Yingying, Qian, Ma, Easton, Mark, Brandt, Milan, 2016. Selective laser melting (slm) of alsil2mg lattice structures. *Mater. Des.* 98, 344–357.
- Li, Yongjie, Yu, Shengfu, Chen, Ying, Yu, Runzhen, Shi, Yusheng, 2020. Wire and arc additive manufacturing of aluminum alloy lattice structure. *J. Manuf. Process.* 50, 510–519.
- Liu, Lu, Kamm, Paul, García-Moreno, Francisco, Banhart, John, Pasini, Damiano, oct 2017. Elastic and failure response of imperfect three-dimensional metallic lattices: the role of geometric defects induced by Selective Laser Melting. *J. Mech. Phys. Solid.* 107, 160–184.
- Liu, Jie, Chen, Tingting, Zhang, Yonghui, Wen, Guilin, Qing, Qixiang, Wang, Hongxin, Sedaghati, Ramin, Yi, Min Xie, 2019. On sound insulation of pyramidal lattice sandwich structure. *Compos. Struct.* 208, 385–394.
- Margerit, P., Weisz-Patrault, D., Ravi-Chandar, K., Constantinescu, A., 2020. Tensile and ductile fracture properties of as-printed 316l stainless steel thin walls obtained by directed energy deposition. Under revision in *Additive Manufacturing*.
- Maskery, I., Aboulkhair, N.T., Aremu, A.O., Tuck, C.J., Ashcroft, I.A., 2017. Compressive failure modes and energy absorption in additively manufactured double gyroid lattices. *Additive Manufacturing* 16, 24–29.
- Nika, Grigor, Constantinescu, Andrei, 2019. Design of multi-layer materials using inverse homogenization and a level set method. *Comput. Methods Appl. Mech. Eng.* 346, 388–409.
- ISO/ASTM 52900:2015, 2015. *Additive Manufacturing — General Principles — Terminology*.
- Ozbilen, Sedat, 1999. Satellite formation mechanism in gas atomised powders. *Powder Metall.* 42, 70–78.
- Philip Bendsoe, Martin, Sigmund, Ole, 2013. *Topology Optimization: Theory, Methods, and Applications*. Springer Science & Business Media.
- Plocher, János, Panesar, Ajit, 2020. Effect of density and unit cell size grading on the stiffness and energy absorption of short fibre-reinforced functionally graded lattice structures. *Additive Manufacturing* 33, 101171.
- Rashed, M.G., Ashraf, Mahmud, Mines, R.A.W., Hazell, Paul J., apr 2016. Metallic microlattice materials: a current state of the art on manufacturing, mechanical properties and applications. *Mater. Des.* 95, 518–533.
- Schumacher, Christian, Bickel, Bernd, Jan, Rys, Marschner, Steve, Daraio, Chiara, Gross, Markus, 2015. Microstructures to control elasticity in 3d printing. *ACM Trans. Graph.* 34 (4), 1–13.
- Sélo, Richard R.J., Catchpole-Smith, Sam, Maskery, Ian, Ashcroft, Ian, Tuck, Christopher, 2020. On the thermal conductivity of alsil0mg and lattice structures made by laser powder bed fusion. *Additive Manufacturing* 34, 101214.
- Sharma, Manish, Dobbstein, Henrik, Thiele, Magnus, Ostendorf, Andreas, 2018. Laser metal deposition of lattice structures by columnar built-up. *Procedia CIRP* 74, 218–221.
- Simon, Mckown, Shen, Y., Brookes, W.K., Sutcliffe, Chris, Cantwell, W.J., Langdon, Genevieve, Nurick, Gerald, Theobald, M.D., 2008. The quasi-static and blast loading response of lattice structures. *Int. J. Impact Eng.* 35, 795–810.
- Sohaib, Z Khan, Masood, S.H., Ryan, Cottam, 2015. Mechanical properties in tensile loading of h13 re-entrant honeycomb auxetic structure manufactured by direct metal deposition. In: *MATEC Web of Conferences*, vol. 34. EDP Sciences, 01004.
- Tancogne-Dejean, Thomas, Spierings, Adriaan B., Mohr, Dirk, 2016. Additively-manufactured metallic micro-lattice materials for high specific energy absorption under static and dynamic loading. *Acta Mater.* 116, 14–28.
- Wang, Xiaoming, Mei, Yulin, Wang, Michael Yu, 2004. Level-set method for design of multi-phase elastic and thermoelastic materials. *Int. J. Mech. Mater. Des.* 1 (3), 213–239.
- Wang, Zhen-Pei, Poh, Leong Hien, Dirrenberger, Justin, Zhu, Yilin, Forest, Samuel, 2017. Isogeometric shape optimization of smoothed petal auxetic structures via computational periodic homogenization. *Comput. Methods Appl. Mech. Eng.* 323, 250–271.
- Wang, Zhen-Pei, Poh, Leong Hien, Zhu, Yilin, Dirrenberger, Justin, Forest, Samuel, May 2019. Systematic design of tetra-petals auxetic structures with stiffness constraint. *Mater. Des.* 170 (C), 107669.
- Xu, Tianqiu, Tang, Shuiyuan, Liu, Changmeng, Li, Zixiang, Fan, Hongli, Ma, ShuYuan, 2020. Obtaining large-size pyramidal lattice cell structures by pulse wire arc additive manufacturing. *Mater. Des.* 187, 108401.
- Yu, Xianglong, Zhou, Ji, Liang, Haiyi, Jiang, Zhengyi, Wu, Lingling, may 2018. *Mechanical Metamaterials Associated with Stiffness, Rigidity and Compressibility: A Brief Review*.
- Yungwirth, Christian J., Radford, Darren D., Aronson, Mark, Wadley, Haydn N.G., 2008. Experiment assessment of the ballistic response of composite pyramidal lattice truss structures. *Compos. B Eng.* 39 (3), 556–569.
- Zhang, Haorui, Huang, Junjin, Liu, Changmeng, Ma, Yongsheng, Han, Yafeng, Xu, Tianqiu, Lu, Jiping, Fang, Hongli, 2020. Fabricating pyramidal lattice structures of 304 l stainless steel by wire arc additive manufacturing. *Materials* 13 (16).